ISSN 2176-5480

22nd International Congress of Mechanical Engineering (COBEM 2013)
November 3-7, 2013, RibeirãoPreto, SP, Brazil

VALIDATION OF CONJUGATE HEAT TRANSFER NUMERICAL METHOD IN REGENERATIVE LIQUID ROCKET ENGINE THRUST CHAMBER

Fausto Ivan Barbosa
Adaiana Francisca Gomes da Silva
Instituto Tecnológico de Aeronáutica (ITA) - Praça Marechal Eduardo Gomes, 50 – Vila das Acácias – S. José dos Campos, SP

barbosafi@yahoo.com, adaiana1@yahoo.com.br

Abstract. *A conjugate convection-conduction numerical method to predict heat transfer in regenerative cooled thrust chamber of liquid rocket engine is described and validated against thermal experimental data. A three dimension simplified model of nozzle, cold water and hot air is built to simulate liquid and gas turbulent flows and systematically assess the effects of grid refinement. A cooled nozzle supersonic flow in a high-enthalpy wind tunnel at Arnold Engineering Development Center (AEDC) provides the comparison data in four different flow conditions. Numerical simulations performed by different authors are also used as assessment base. Results indicate that this study can be an effective method for predicting the flow and heat transfer in regenerative cooled thrust chamber.*

Keywords: *liquid propulsion, liquid rocket engine, rocket propulsion*

NOMENCLATURE

C_1 = constant;
C_2 = variable;
c_p = specific heat;
G_k = generation of turbulence kinetic energy due to the mean velocity gradients;
h = enthalpy;
k = turbulence kinetic energy;
p = static pressure;
Pr_t = turbulent Prandtl number;
S_h = energy sources;
t = time;
T = static temperature;
ΔT = difference in temperature between two points;
u_i and x_i = Cartesian velocity and direction components;
v = velocity intensity;
Y_M = contribution of the fluctuating dilatation in compressible turbulence to the overall dissipation rate;
ε = dissipation rate of turbulence kinetic energy;
λ = thermal conductivity;
ρ = density;
τ = stress tensor;
σ_k and σ_ε = turbulent Prandtl numbers for k and ε, respectively;
μ = viscosity of the fluid;
μ_t = turbulent (or eddy) viscosity;
$\tilde{\tilde{\Omega}}_{ij}$ = mean rate of rotation tensor viewed in a moving reference frame with an angular velocity ω_k.

1. INTRODUCTION

Computational Fluid Dynamics (CFD) has been a useful method to simulate the flow behavior in several situations to satisfy the user's needs, especially due to accelerated advances in computational technologies. Most existing CFD and heat transfer codes require that either the wall temperature or the wall heat flux be specified as a boundary condition. However, both of these are unknown without a complete simultaneous analysis of the heat transfer problem within gas, solid and coolant.

A comprehensive thermal analysis of regenerative-cooled liquid rocket engine thrust chambers has been strongly benefited by the popularization of CFD techniques, assuring the theoretical integrity of the thrust chamber. Adequate

ISSN 2176-5480

understanding and accurate prediction of heat transfer in the hot gas, chamber wall and coolant is prerequisite of thrust chamber reusable design. The continuous demand of higher performance engines has resulted in higher pressure and temperature for the thrust chambers and the need for more sophisticated cooling methods, such as regenerative cooling.

Shope (1994) developed and extensively modified a space-marching boundary layer program to model conjugate conduction-convection heat transfer for the case of co-flowing high-speed gas and liquid coolant. Solid body conduction was modeled as one-dimensional, constant property heat transfer. The coolant was modeled empirically as a bulk fluid with combined forced convection and sub-cooled nucleate boiling. The flow solver was modified to solve the group of conjugate boundary equations simultaneously and implicitly with the existing momentum and energy equations for the gas. The theoretical water coolant temperature rise was shown to agree quite well with the measured temperature rise and nucleate boiling is predicted to be crucial effect of coolant.

Engblom *et al.* (2007 and 2008) created a structured-grid heat transfer module coupled with two different compressible Reynolds-Averaged Navier-Stokes flow solvers and predictions were compared to experimental data for various turbulence models and coolant modeling assumptions. A finite-volume, cell-centered, multi-block structured-grid, heat flow solver with sub-models for solid body conduction, forced convection, nucleate and film boiling. These sub-models were configured for analysis of water-cooled high seed flows. Temperature gradient of solid was evaluated at each cell face using 2nd order spatial treatment. Coolant flow was treated as a separate three-dimensional zone which exchanges heat with one solid body zone. The nucleate boiling heat is a relevant mechanism when coolant temperatures reach liquid saturation conditions.

Kang and Sun (2011) simulated the hot gas convective and radiative heat transfer separately from the conjugate heat transfer in the coolant and cooling channel in order to prevent numerical instability. A common inner wall temperature was used to assure the balance of heat flux at gas-solid interface, coupling both domains. Standard wall function was used to bridge the viscosity affected region between the wall and the fully turbulent region. RMS turbulence model was used to model the turbulent air and water flow. Frozen flow and non-equilibrium (finite rate) flow were compared showing less heat flux in the first case.

This article presents a conjugate convection-conduction numerical simulation a three dimension simplified model of a water-cooled supersonic nozzle. Simulations results were compared with tests performed in a high-enthalpy wind tunnel facility at Arnold Engineering Development Center (AEDC), placed at Arnold Air Force Base, Tenessee, USA, for several gas and coolant flow conditions.

2. PHYSICAL DESCRIPTION

2.1 Test device

According to Shope (1994), experiments were performed in a device consisting of a 40 MW segmented electric arc-heated high enthalpy ablation test unit. In such unit, air at 68 atm is continuously heated by passing through an electric arc placed inside a column of 5 cm diameter and about 2 m long. The heated air is expanded through water cooled, double shell, convergent-divergent, supersonic nozzle designed to provide a region of uniform flow, as shown is Fig. 1.

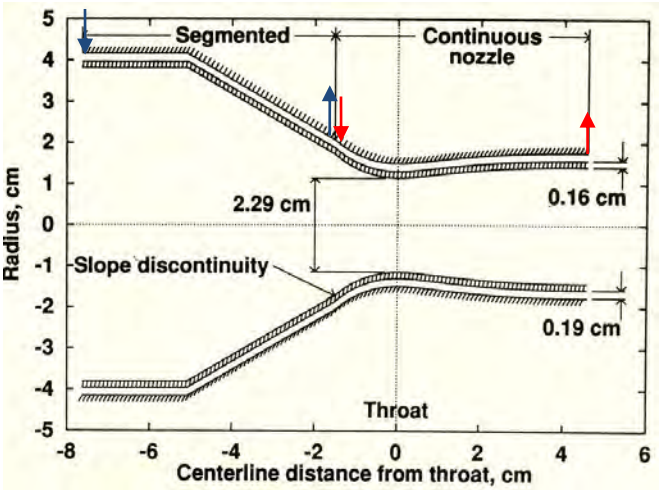

Figure 1. Nozzle geometry as modeled. (Source: Shope, 1994)

ISSN 2176-5480

The inner shell is made of a copper-zirconium alloy with 0.16 cm wall thickness and geometry consisting of inlet of 7.6 cm diameter and throat of 2.29 cm diameter. Between the inner and outer shells, coolant water flows confined into a narrow channel of 0.19 cm height. The convergent part has a conical geometry and, after the throat, takes place the divergent part with bell geometry designed for parallel exit velocity at Mach number 1.8.

The device is divided in two segments and each of them has its own water inlet and outlet. The overall length of the continuous nozzle segment is 5.8 cm. The inlet of the first segment is placed at the beginning of the device and the outlet is at upwind the throat. Near the same point, it is placed the inlet of the second segment which outlet is located at the end of the nozzle. Water inlet and outlet of the first and second segments are illustrated with blue and red arrows.

2.2 Test conditions

The cases consist of four different flow conditions, depending on the air total pressure and total temperature, as well as water mass flow rate and inlet temperature of the water, as shown in Tab. 1.

Table 1. Air and water flow conditions for the test cases (Source: Shope, 1994)

	Case #1	Case #2	Case #3	Case #4
Air total pressure, atm	126,5	137,0	104,4	94,3
Air total temperature, K	5000	5240	4600	5100
Water mass flow rate, kg/s	5,234	5,234	3,216	3,204
Water inlet temperature, K	309	307	289	289

2.3 Material properties

Properties of all materials used in the simulations are listed in the Tab. 2. Constant gas properties were calculated as air in chemical equilibrium at defined pressure and temperature according to the gas inlet conditions.

Table 2. Constant properties of gas, liquid and solid materials

	Gas (air)				Liquid (water)	Solid (Cu-Zr)
	Case #1	Case #2	Case #3	Case #4	All cases	All cases
Density, kg/m^3	Ideal gas	Ideal gas	Ideal gas	Ideal gas	998,2	8978
Specific heat, J/(kg*K)	1331,41	1332,42	1326,40	1333,00	4182	381
Thermal conductivity, W/(m*K)	0,210	0,219	0,196	0,215	0,6	387,6
Viscosity, kg/(m*s)	0,000124	0,000128	0,000117	0,000126	0,001003	-
Molar weight, kg/mol	26,68	26,34	27,26	26,28	-	-

Figure 2 presents the dependence of some variable gas properties of the temperature, considering two different pressures. One can note that such properties are not so influenced by the pressure, as well as can be approximated by linear simple expressions. Simulations with variable gas properties were performed with properties at 126 bar.

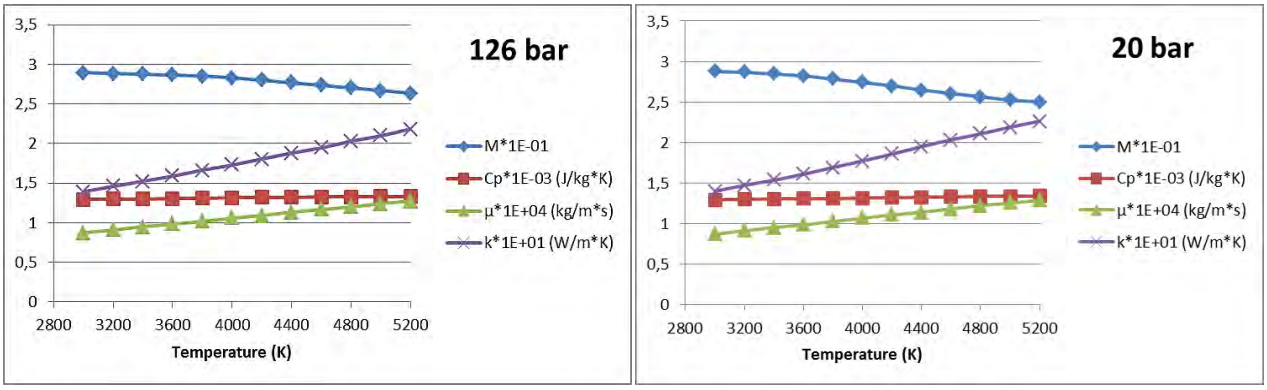

Figure 2. Variable gas properties depending on the temperature and pressure

ISSN 2176-5480

3. MATHEMATICAL MODEL

A compressible ideal gas and incompressible liquid flows, both in steady state, subjected to a conjugate convection-conduction heat transfer process were considered. The gas was modeled with constant and variable thermodynamical properties, dependent on the temperature. Chemical kinetics related to the dissociation and recombination of species in the hot air was not considered, consequently, energy source was neglected.

The main governing equations to be solved are:

a) The continuity equation:

$$\frac{\partial}{\partial x_j}\left(\rho u_j\right)=0 \tag{1}$$

where ρ is the density, u_j and x_j are respectively the Cartesian velocity and direction components.

b) The momentum equations (see RANS model and Boussinesq hypothesis in Ansys Fluent Theory Guide, 2010):

$$\frac{\partial}{\partial x_j}\left(\rho u_i u_j\right)=-\frac{\partial p}{\partial x_i}+\frac{\partial}{\partial x_j}\left[\left(\tau_{ij}\right)_{eff}-\frac{2}{3}\rho k\delta_{ij}\right] \tag{2}$$

$$\left(\tau_{ij}\right)_{eff}=\mu_{eff}\left(\frac{\partial u_j}{\partial x_i}+\frac{\partial u_i}{\partial x_j}-\frac{2}{3}\frac{\partial u_k}{\partial x_k}\delta_{ij}\right);\quad \mu_{eff}=\mu+\mu_t \tag{3}$$

where: ρ is the density, p is the static pressure, μ is the dynamic viscosity, u_i and x_i are respectively the Cartesian velocity and direction components, μ_t is the turbulent (eddy) viscosity, k is the turbulence kinetic energy.

c) The energy equation:

$$\frac{\partial}{\partial x_j}\left[\left(\rho E+p\right)u_j\right]=\frac{\partial}{\partial x_j}\left[\lambda_{eff}\frac{\partial T}{\partial x_j}+u_i\left(\tau_{ij}\right)_{eff}\right] \tag{4}$$

$$E=h-\frac{p}{\rho}+\frac{v^2}{2};\quad \lambda_{\text{eff}}=\lambda+\lambda_t;\quad \lambda_t=\frac{c_p\,\mu_t}{\text{Pr}_t};\quad \text{Pr}_t=0.85 \tag{5}$$

where ρ is the density, p is the static pressure, λ is the thermal conductivity, c_p is specific heat, Pr_t is the turbulent Prandtl number, T is the static temperature, u_i and x_i are respectively the Cartesian velocity and direction components, h is the enthalpy, v is the velocity intensity, S_h includes the heat of chemical reaction and other energy sources.

d) The transport equations (see Realizable *k-ε* model in in Ansys Fluent Theory Guide, 2010):

$$\frac{\partial}{\partial x_j}\left(\rho k u_j\right)=\frac{\partial}{\partial x_j}\left[\left(\mu+\frac{\mu_t}{\sigma_k}\right)\frac{\partial k}{\partial x_j}\right]-\rho\varepsilon+G_k-Y_M \tag{6}$$

$$\sigma_k=1.0;\quad G_k=\mu_t S^2;\quad S=\sqrt{2S_{ij}S_{ij}};\quad S_{ij}=\frac{1}{2}\left(\frac{\partial u_j}{\partial x_i}+\frac{\partial u_i}{\partial x_j}\right);\quad Y_M=2\rho\varepsilon M_t^2;\quad M_t=\sqrt{\frac{k}{\gamma RT}} \tag{7}$$

$$\frac{\partial}{\partial x_i}\left(\rho\varepsilon u_i\right)=\frac{\partial}{\partial x_j}\left[\left(\mu+\frac{\mu_t}{\sigma_\varepsilon}\right)\frac{\partial\varepsilon}{\partial x_j}\right]+\rho C_1 S\varepsilon-\rho C_2\frac{\varepsilon^2}{k+\sqrt{\nu\varepsilon}} \tag{8}$$

$$\sigma_\varepsilon=1.2;\quad C_1=\max\left[0.43,\frac{\eta}{\eta+5}\right];\quad \eta=S\frac{k}{\varepsilon};\quad C_2=1.9 \tag{9}$$

ISSN 2176-5480

where k is turbulence kinetic energy; ε is the dissipation rate of turbulence kinetic energy; μ is the dynamic viscosity; μ_t is the turbulent (eddy) viscosity; G_k is the generation of turbulence kinetic energy due to the mean velocity gradients; Y_M is the contribution of the "dilatation dissipation" in compressible turbulence to the overall dissipation rate; σ_k and σ_ε are the turbulent Prandtl numbers for k and ε, respectively; C_1 is variable and C_2 is constant.

e) The turbulent (or eddy) viscosity:

$$\mu_t = \rho C_\mu \frac{k^2}{\varepsilon} \tag{10}$$

$$C_\mu = \frac{1}{A_0 + A_S \dfrac{kU^*}{\varepsilon}}; \quad A_0 = 4.04; \quad A_S = \sqrt{6}\cos\phi; \quad \phi = \frac{1}{3}\cos^{-1}\left(\sqrt{6}W\right); \quad W = \frac{S_{ij}S_{jk}S_{ki}}{\bar{S}^3}; \quad \bar{S} = \sqrt{S_{ij}S_{ij}} \tag{11}$$

$$S_{ij} = \frac{1}{2}\left(\frac{\partial u_j}{\partial x_i} + \frac{\partial u_i}{\partial x_j}\right); \quad U^* = \sqrt{S_{ij}S_{ij} + \tilde{\Omega}_{ij}\tilde{\Omega}_{ij}}; \quad \tilde{\Omega}_{ij} = \Omega_{ij} - 2\varepsilon_{ijk}\omega_k; \quad \Omega_{ij} = \bar{\Omega}_{ij} - \varepsilon_{ijk}\omega_k \tag{12}$$

Where $\bar{\Omega}_{ij}$ is the mean rate-of-rotation tensor viewed in a moving reference frame with an angular velocity ω_k.

f) The near-wall model:

Enhanced wall treatment is a near-wall modeling method that combines a two-layer model with so-called enhanced wall functions. If the near-wall mesh is fine enough to be able to resolve the viscous sub-layer (typically with the first near-wall node placed at y+ ≈ 1), then the enhanced wall treatment will be identical to the traditional two-layer zonal model. However, the restriction that the near-wall mesh must be sufficiently fine everywhere might impose too large a computational requirement.

Ideally, one would like to have a near-wall formulation that can be used with coarse meshes (usually referred to as wall-function meshes) as well as fine meshes (low-Reynolds-number meshes). In addition, excessive error should not be incurred for the intermediate meshes where the first near-wall node is placed neither in the fully turbulent region, where the wall functions are suitable, nor in the direct vicinity of the wall at y+ ≈ 1, where the low Reynolds-number approach is adequate.

To achieve the goal of having a near-wall modeling approach that will possess the accuracy of the standard two-layer approach for fine near-wall meshes and that, at the same time, will not significantly reduce accuracy for wall-function meshes, one can combine the two-layer model with enhanced wall functions, as described in Ansys Fluent Theory Guide (2010).

4. COMPUTATIONAL MODEL

4.1 Grid description

Grids were prepared in three different resolutions consisting of fine, base and coarse grids, as shown in Tab. 3. Such grids were obtained by cut-cell meshing method, suitable to create cells with low deformity. Near the walls, meshes were gradually refined at the gas and liquid sides using the inflation method, in order to capture the boundary layer.

Table 3. Grid resolutions

	Grid #1 (fine)	Grid #2 (base)	Grid #3 (coarse)
Quantity of cells	139997	79860	24370

The problem was modeled as a multi-body part with only 3.75° azimuthal slice of the nozzle, including hot gas, chamber wall and coolant regions, as shown in Fig. 3.

ISSN 2176-5480

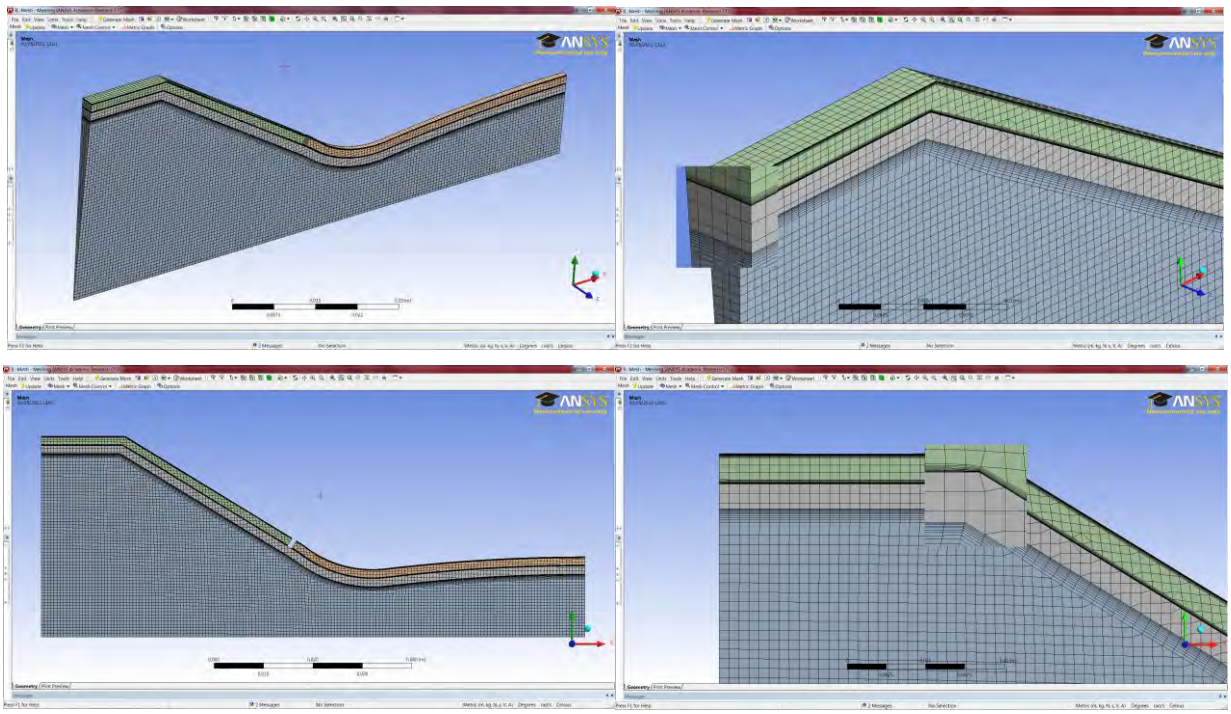

Figure 3. Grid details

4.2 Numerical settings

Simulations were performed with the software ANSYS Workbench - Fluent, a state-of-art computer program for modeling and solving fluid flow and heat transfer in complex geometries.

The model was simulated using the pressure-based scheme and the Simple pressure-velocity coupling method. To assure the compromise between the solution stability and computational efforts, under-relaxation factors were set as follows: 0.3 for pressure; 0.7 for momentum; 0.8 for turbulence kinetic energy and turbulence dissipation rate; 1.0 for density, body forces, energy and turbulent viscosity. In order to decrease false diffusion effects, spatial discretization was set as follows: least squares cell based for gradient; second order for pressure; second order upwind for density, momentum, energy, turbulent kinetic energy, and turbulent dissipation rate. The initial thermodynamical properties of the air were assumed to be in chemical equilibrium at the nozzle inlet.

Boundary conditions were defined as:

a) prescribed gauge total temperature and gauge total pressure at the gas inlet,
b) prescribed gauge static pressure and backflow total temperature at the gas outlet,
c) prescribed mass flow rate and total temperature at the coolant inlet for both segments,
d) zero heat flux (adiabatic wall) at the coolant outside for both segments,
e) zero flux for all flow variables and overall mass balance correction (outflow) at coolant outlet for both segments,
f) prescribed zero heat flux (adiabatic wall) at the front and back of the chamber wall,
g) zero normal velocity and zero normal gradients of all flow variables (symmetry) at the lateral planes.

Coolant mass flow rate was simulated as 1/96 of the total mass flow rate to be compatible with the azimuthal slice of the nozzle. Turbulence parameters were set considering 5% turbulent intensity and 10% turbulent viscosity ratio.

The stabilization of the pressure and temperature at the second channel throat and outlet, as well as at the nozzle throat and outlet, were used as convergence criteria. In these simulations, residues of the equations of continuity, x-velocity, y-velocity, z-velocity, energy, turbulent kinetic energy and turbulence dissipation rate reached more than four orders.

ISSN 2176-5480

5. RESULTS AND DISCUSSIONS

5.1 Grid selection

Flows with constant and variable gas properties were simulated considering three different grid resolutions and four initial conditions. Simulation results were compared with the AEDC experiment results in terms of coolant bulk temperature rise in the second segment of the nozzle.

The difference of coolant bulk temperature rise between the simulations and experiments were organized in the Tab. 4. Simulations show that coolant bulk temperature rises in the cases with variable gas properties are smaller than those with constant gas properties, considering all of the grids and cases.

Table 4. Coolant bulk temperature rise depending on the grids resolutions

		Case #1	Case #2	Case #3	Case #4
Experimental results	ΔT (K)	13,9	15,0	18,9	20,0
Grid #1 - constant gas properties	ΔT (K)	13,5	15,4	17,1	17,7
Grid #1 - variable gas properties	ΔT (K)	12,5	14,1	16,0	16,0
Grid #2 - constant gas properties	ΔT (K)	13,6	14,8	17,1	17,7
Grid #2 - variable gas properties	ΔT (K)	12,6	13,7	16,1	16,2
Grid #3 - constant gas properties	ΔT (K)	16,3	17,8	17,6	19,6
Grid #3 - variable gas properties	ΔT (K)	15,1	16,4	16,2	17,6

The deviations of coolant bulk temperature rise with respect to the experiments are presented in terms of percentage in Fig. 4. The “zero percent line” represents the experimental results for the coolant bulk temperature rise. Simulations show that errors in coolant bulk temperature rises have conformity between grid #1 and grid #2, but not with grid #3.

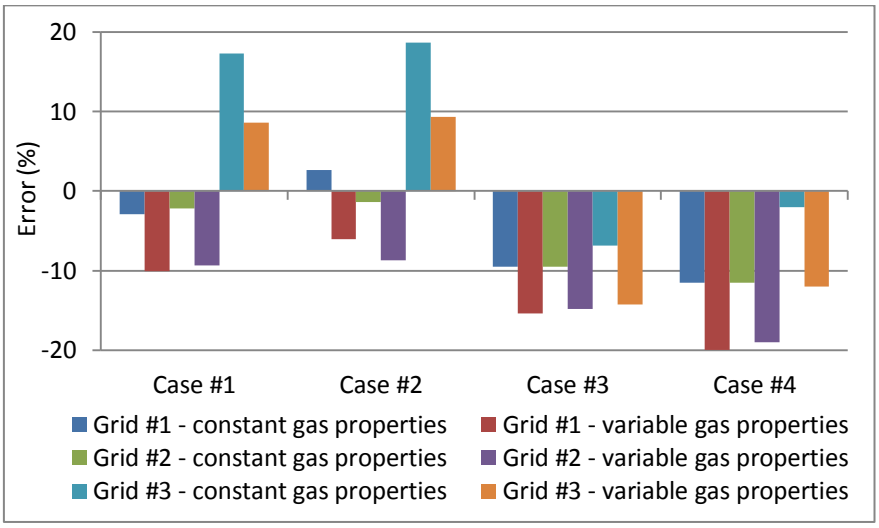

Figure 4. Errors depending on the grid resolutions

Considering that the two finer grids #1 and #2 showed results with a similar tendency and small differences between them, and weighting the computational cost, the grid #2 was chosen as the most appropriate and will be used present some results.

5.2 Comparative results

For comparison purposes, Tab. 5 shows the coolant bulk temperature rise in the experiment and simulation cases found in several articles. Results of this article were satisfactory in comparison with other assessed works. For the cases #1 and #2, simulation results obtained with constant gas properties were the best of all, and for the cases #3 and #4, they stayed around the average.

ISSN 2176-5480

Table 5. Coolant temperature rise according to the references

		Case #1	Case #2	Case #3	Case #4
Experimental results	ΔT (K)	13,9	15,0	18,9	20,0
Shope, 1994	ΔT (K)	14,3	16,3	18,0	19,6
Engblom *et al.*, 2007[#]	ΔT (K)	13,3	14,8	18,1	18,0
Engblom *et al.*, 2007[##]	ΔT (K)	12,8	14,1	16,6	16,6
Engblom *et al.*, 2008	ΔT (K)	13,1	14,5	16,2	17,5
Kang and Sun, 2011[*]	ΔT (K)	12,3	13,5	15,5	15,7
Kang and Sun, 2011[**]	ΔT (K)	14,5	16,1	17,5	18,5
Barbosa and Silva, 2013[+]	ΔT (K)	13,6	14,8	17,1	17,7
Barbosa and Silva, 2013[++]	ΔT (K)	12,6	13,7	16,1	16,2

[#]nucleate boiling
[##]nucleate and film boiling
[*]frozen flow
[**]non-equilibrium flow
[+]constant gas properties
[++]variable gas properties

The deviations of coolant bulk temperature rise with respect to the experiments are presented in terms of percentage in Fig. 5, comparing with other works. As in Fig. 4, the "zero percent line" represents the experimental coolant bulk temperature rise. Simulations show that errors in the coolant bulk temperature rises have qualitative agreement with most of the works, particularly when using constant gas properties.

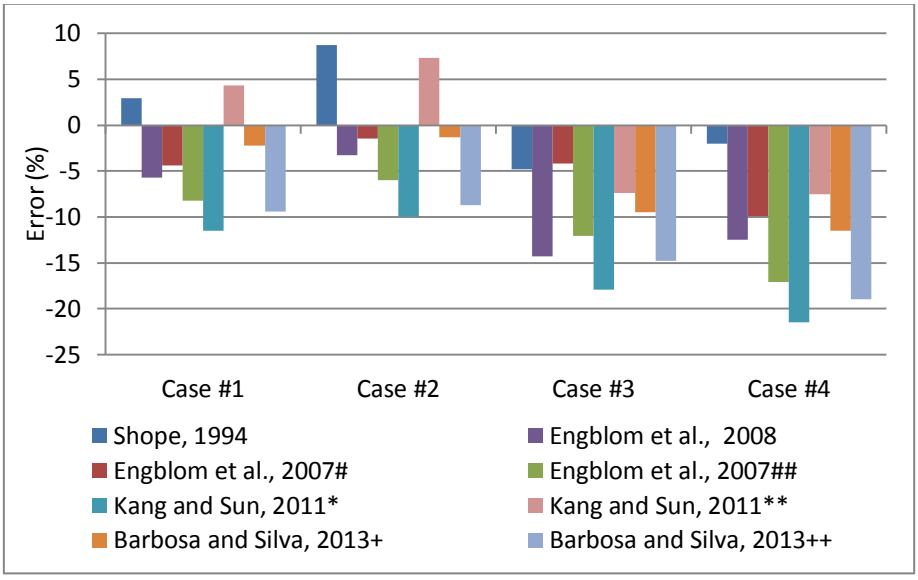

Figure 5. Errors according to the references

5.3 Extended results

Figure 6 shows the gas side heat flux along the axial direction, with both constant and variable gas properties, for the selected grid #2. Note that all of the results presented the same behavior, with a peak slightly upstream the throat and with constant gas properties always higher than the variable gas properties. Gas-side heat flux for the cases #1 and #2 are higher than for the cases #3 and #4.

ISSN 2176-5480

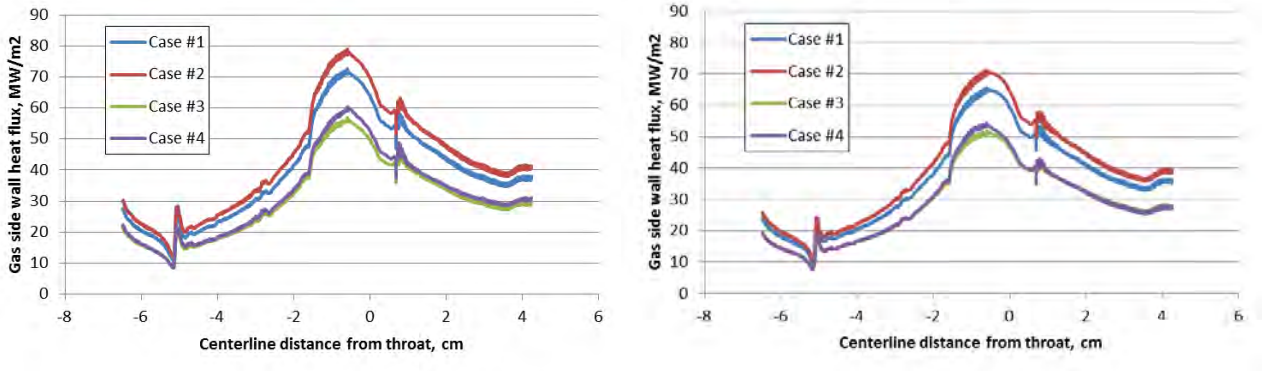

Figure 6. Gas side wall heat flux (left: constant gas properties; right: variable gas properties)

Figure 7 shows the gas side wall temperature along the axial direction, with both constant and variable gas properties, for the selected grid #2. Note that all of the results presented the same behavior, with an expected peak slightly upstream the throat and with constant gas properties always higher than the variable gas properties. Gas-side wall temperature for the cases #2 and #4 are higher than for the cases #1 and #3.

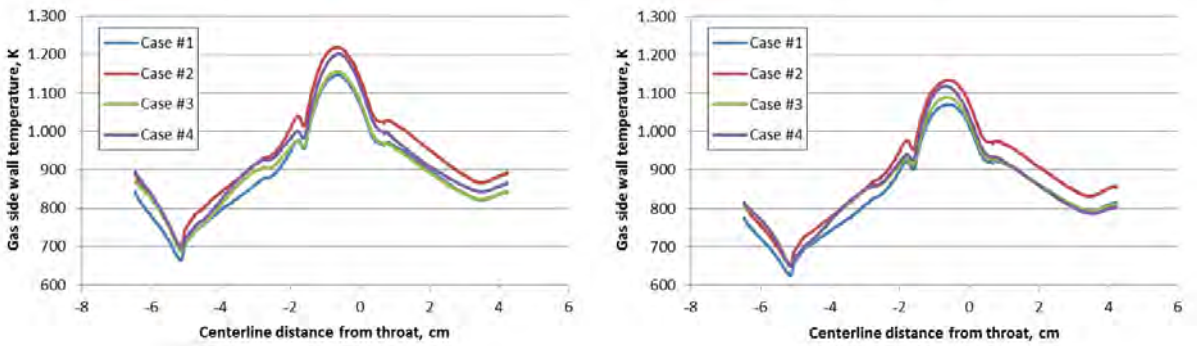

Figure 7. Gas side wall temperature (left: constant gas properties; right: variable gas properties)

Both Figures 6 and 7 shows increasing values at the nozzle boarders. Such effect reflects the influence of the chosen boundary condition, set as adiabatic wall at the front and back chamber wall, which overloads the heat transfer near those regions.

6. REFERENCES

Ansys Fluent Theory Guide. Release 13.0. November 2010. <http://www.ansys.com/Support/Documentation>.

Engblom, W., Fletcher, B. and Georgiadis, N., 2007. "Validation of conjugate heat-transfer capability for water-cooled high-speed flows". In *Proceedings of the 39th AIAA Thermophysics Conference – AIAA 2007-4392*. Miami, FL.

Engblom, W., Fletcher, B. and Georgiadis, N., 2008. "Conjugate conduction-convection heat transfer for water-cooled high-speed flows". In *Proceedings of the 44th AIAA/ASME/SAE/ASEE Joint Propulsion Conference & Exhibit – AIAA 2008-4653*. Hartford, CT.

Kang, Y. D. and Sun, B., "Numerical simulation of liquid rocket engine thrust chamber regenerative cooling", *Journal of Thermophysics and Heat Transfer*, Vol. 25, No. 1, January-March 2011, pp 155 – 164.

Shope, F. L., "Conjugate conduction-convection heat transfer with a high-speed boundary layer", *Journal of Thermophysics and Heat Transfer*, Vol. 8, No. 2, April-June 1994, pp 275 – 281.

7. RESPONSIBILITY NOTICE

The authors are the only responsible for the printed material included in this paper.